Bulletin of the Seismological Society of America, Vol. 104, No. 1, pp. –, February 2014, doi: 10.1785/0120130088

Ground Motion in the Presence of Complex Topography: Earthquake and Ambient Noise Sources

by Stephen Hartzell, Mark Meremonte, Leonardo Ramírez-Guzmán, and Daniel McNamara

Abstract To study the influence of topography on ground motion, eight seismic recorders were deployed for a period of one year over Poverty Ridge on the east side of the San Francisco Bay Area, California. This location is desirable because of its proximity to local earthquake sources and the significant topographic relief of the array (439 m). Topographic amplification is evaluated as a function of frequency using a variety of methods, including reference-site-based spectral ratios and single-station horizontal-to-vertical spectral ratios using both shear waves from earthquakes and ambient noise. Field observations are compared with the predicted ground motion from an accurate digital model of the topography and a 3D local velocity model. Amplification factors from the theoretical calculations are consistent with observations. The fundamental resonance of the ridge is prominently observed in the spectra of data and synthetics; however, higher-frequency peaks are also seen primarily for sources in line with the major axis of the ridge, perhaps indicating higher resonant modes. Excitations of lateral ribs off of the main ridge are also seen at frequencies consistent with their dimensions. The favored directions of resonance are shown to be transverse to the major axes of the topographic features.

Introduction

Topography has long been known to modify observed surface ground motions. Sato (1955) considered the superposition of plane waves to investigate reflected waves from a corrugated free surface. Aki and Larner (1970) introduced a frequency domain method to study irregularly shaped interfaces imbedded in a half-space. Large recorded motions from the 1971 San Fernando, California, earthquake, particularly at the Pacoima Dam site, stimulated interest in the effects of topography. Bouchon (1973) applying an extension of the Aki and Larner (1970) method and Boore (1972) using finite difference, both considered simple 2D topography and concluded that significant amplification occurs at topographic highs for incident wavelengths comparable to the width of the topographic feature. Correspondingly, deamplification occurs at topographic depressions. Bard (1982) further considered the effects of incident wave type, frequency, incidence angle, and anomaly height. Systematically greater amplification was found for incident S waves than for P waves. Amplification was also shown to increase with increasing slope of the topographic high and decreasing angle of incidence. Geli *et al.* (1988) provided a useful summary of theoretical and observed amplification values as well as additional calculations for 2D structures with subsurface layering and neighboring topographic features. Their crest-to-base spectral amplification values range up to a factor of 10 or more. Amplification at the crest of topography was shown to be a maximum for a frequency of c/l, in which c is the material velocity and l is the base width of the topographic feature. The compilation of available data showed that numerical simulations often underestimate observed amplification, which was related to the difficulty of isolating topographic effects from other site effects and the two-dimensionality often assumed in the numerical calculations. Sánchez-Sesma and Campillo (1991) developed a boundary integral method and simulated topographic effects for a variety of hypothetical features in a half-space. They found relative amplifications that can be greater than 10 due to complicated patterns of amplification and deamplification but that absolute levels of amplification were generally lower than about four times the amplitude of the incoming wave. They stressed the large variability of spectral content of ground motion in both frequency and space. Bouchon *et al.* (1996) developed a semianalytical seminumerical method to calculate the diffraction of seismic waves by 3D topography of arbitrary shape. Since then, fully numerical finite-element methods have dominated the simulation of topographic effects in 3D media. Ma *et al.* (2007) showed that mountains produce a shielding effect by the scattering of predominantly surface waves, resulting in lower ground motions in the region beyond the topography. Lee, Chan, *et al.* (2009) and Lee, Komatitsch, *et al.* (2009) found that topography can change peak ground velocity in mountainous areas by ±50%

compared to a half-space, and the relative change in peak ground acceleration between a valley and a ridge can be as high as a factor of 2. Shaking was also found to be strongly dependent on the scale of the topographic features in relation to the wavelength of the source content.

These theoretical investigations have been complemented by the analysis of recorded motions over topographic features. Davis and West (1973) calculated crest-to-base ratios in the time and frequency domains for three mountains in southern California and Nevada using aftershocks of the 1971 San Fernando earthquake and a cavity collapse following a Nevada Test Site (NTS) detonation. In general, the wavelengths corresponding to the maximum amplifications are comparable to the mountain widths, consistent with theory, but the observed amplifications are much larger. Rogers *et al.* (1974) considered only time-domain crest-to-base amplitude ratios for another NTS explosion. Their observed amplitude ratios were consistent with theory, perhaps aided by the simple geometry of the topography and source alignment. Griffiths and Bollinger (1979) also only used time-domain crest-to-base amplitude ratios across the approximately 2D topography of the Appalachian Mountains and sources from mainly quarry and mine blasts. They observed a large scatter in values with an average amplification significantly larger than theoretical predictions. Pedersen *et al.* (1994) obtained general agreement between observations and simulations for amplification over a simple ridge in Greece. They conclude that topographic deamplification at a reference site can lead to overestimation of ridge-crest amplification compared to theoretical predictions. Studies of aftershocks of the 1994 Northridge, California, earthquake on a hill in Tarzana, prompted by large mainshock ground motions, pointed out the directional seismic response of the hill that results in a strong amplification of ground motion transverse to the direction of elongation of the hill (Bouchon and Barker, 1996; Spudich *et al.*, 1996). Massa *et al.* (2010) instrumented a ridge in central Italy and calculated horizontal-to-vertical-component spectral ratios (HVSRs) and the ridge-crest-to-base spectral ratios for small local earthquakes. Results from the reference site crest-to-base spectral ratios were considered to be more accurate. Amplification factors increased when the direction of ground motion was perpendicular to the ridge elongation. Panzera *et al.* (2011) advocated the use of HVSR using ambient noise sources to study topographic effects on a raised peninsula on Sicily. They found HVSR desirable because it avoided the difficulty of finding a reference site free of topographic effects. They showed a consistency between HVSR analysis and polarization analysis in the directional effect having an azimuth transverse to the major axis of the peninsula.

Despite these studies, there are still lingering questions about the reliability of theoretical calculations in the evaluation of topographic effects and the appropriateness of earthquake versus ambient noise sources and the types of data analysis. In this paper, we combine analysis of ground-motion recordings from a field study in a mountainous region of the San Francisco Bay Area, California, with full 3D finite-element simulations using an accurate 10 m digital elevation model (DEM). Although data and theory have been compared in several previous investigations, as referenced previously, earlier studies mostly have used simplistic 2D models to represent complicated real-world conditions. In the processing of the ground-motion records, we compare reference-site-based spectral ratios with HVSR for local earthquake sources. We also compute HVSR using ambient noise and investigate the directionality characteristics of the site amplification.

Study Area and Seismic Stations

The field deployment consists of eight stations in two separate lines of four stations each, straddling Poverty Ridge in the Diablo Mountains east of San Jose, California (Fig. 1; Table 1). This location was selected for our investigation of topographic effects for three reasons: (1) its proximity to the Calaveras fault, 3.5 km to the west, which is the source of numerous small earthquakes; (2) the approximate linear trend of the ridge, striking 140° from north; and (3) the significant topographic relief, rising 500 m above the Arroyo Hondo River on its east side in about 1.25 km. Instrumentation included Compact Trillium seismometers and RefTek recorders with two recording modes: continuous at 40 samples/s and triggered at 100 samples/s. The sensor was buried in a small vault approximately 20 cm below the ground surface. Deployment was for one year from June 2011–2012. During this period, 43 local earthquakes with a magnitude greater than 2.4 were recorded at one or more stations. Table 2 lists 27 of these that were recorded by at least seven stations and are the subject of more detailed analysis because of their better station coverage. Figure 1c shows the epicenters of the closer sources to Poverty Ridge, which follow the trend of the Calaveras fault, with numerical labels from Table 2 for the events receiving special consideration in this study.

Because of the recognized difficulty of distinguishing topographic effects from other site effects resulting from soft surficial deposits, a discussion of the local setting of each instrument is appropriate and useful for our interpretation of the data. Figure 2 shows the location of the two lines of stations across Poverty Ridge. The ridge is composed of Franciscan Complex metamorphic rocks of Cretaceous age. Each sensor, except the two ridge-crest sites (RDG13 and RDG23), was placed in contact with a rock outcrop or within approximately 2 m of a rock outcrop on fractured material from the same unit. Hard rock is not visible in the immediate vicinity of the ridge crest sites because of the development of a soil layer. However, rock is seen in road cuts at an elevation of a few meters below the top of the ridge. Most of our observations in this paper lie below a frequency of 3 Hz. For a spectral peak at 3 Hz to have its origin from a shallow resonance would require a sediment thickness of 25 m for a shear-wave velocity of 300 m/s. The general absence of thick sediments at the station locations should make it possible to identify the uncontaminated topographic effects.

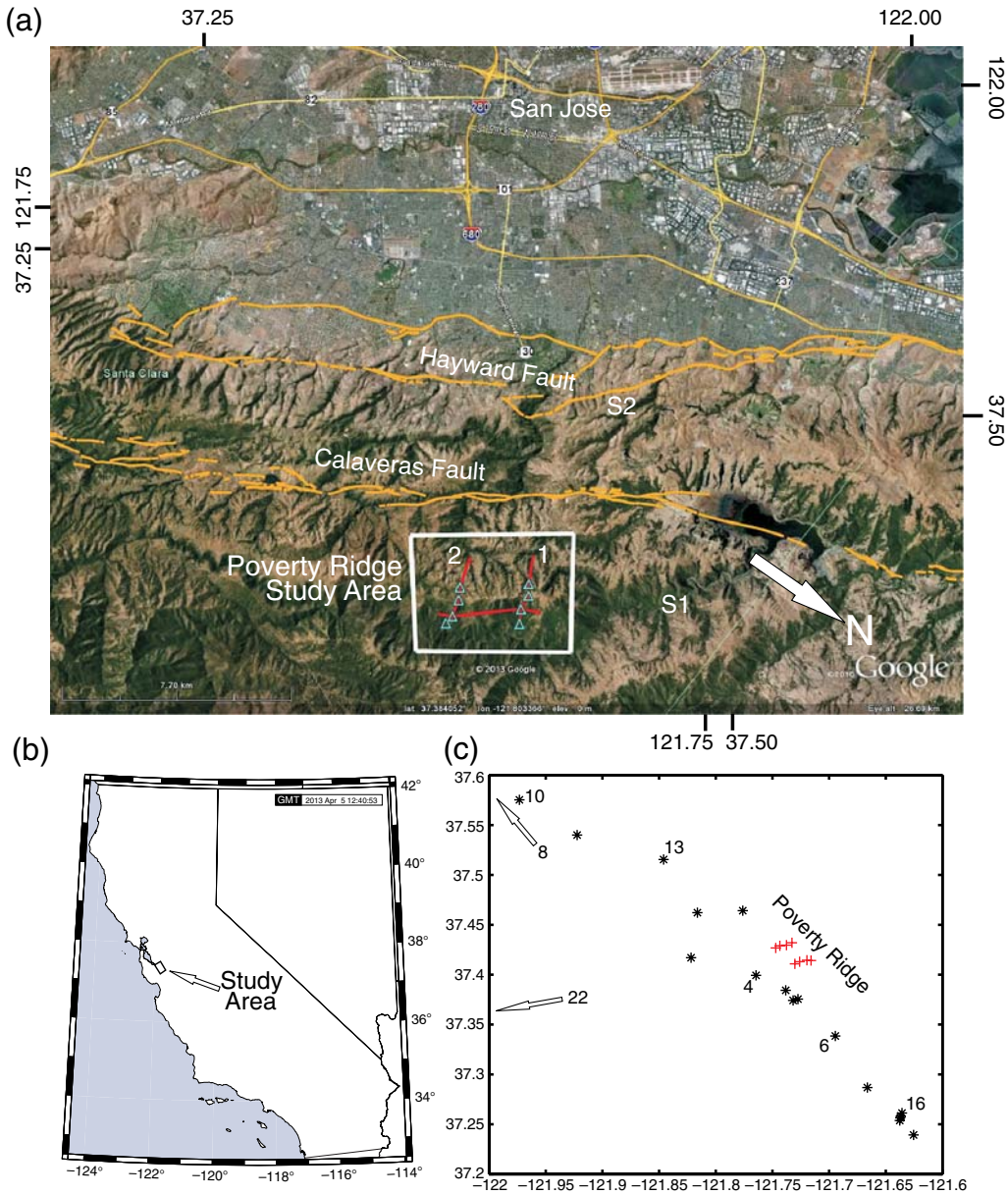

Figure 1. (a) The Poverty Ridge study area in the Diablo Mountains on the east side of the Santa Clara Valley, California. Locations of the two seismograph station lines (labeled 1 and 2) are shown within the rectangular box. Individual stations are indicated by triangles. Lines through the stations and a third line parallel to the ridge axis on its northeast side show the locations of topographic profiles in Figure 2. S1 and S2 are locations of two simulated earthquake sources. (b) A regional location map of the study area. (c) A location map of the closer earthquake sources to Poverty Ridge used in this study, with numerical labels from Table 2 for the events of special consideration. Events 8 and 22 lie off the map in the directions indicated by the arrows. The trend of epicenters follows the Calaveras fault. Station locations are indicated by plus symbols. The color version of this figure is available only in the electronic edition.

This argument is bolstered by our synthetic modeling results, presented later, that fit the observations well without the effects of any near-surface layering.

Figure 2 shows the complexity of the topography on Poverty Ridge, which is characterized by erosional gullies on the western and eastern sides of the main ridge. These features form secondary ridges approximately perpendicular to the main ridge (Fig. 2c). Thus, we expect to see more than one characteristic mode of excitation related to the topographic features of different sizes.

Observational Results

Earthquake Ground Motions with Reference-Site-Based Method

We first consider the response of 43 local earthquakes having good signal-to-noise amplitude at the array stations. The shear waves, including coda, are windowed from the records. These record sections vary in length from 20 to 35 s depending on the magnitude of the earthquake. No corrections are needed for geometrical spreading or attenuation

Table 1
Station Locations

Name	Latitude (°)	Longitude (°)	Elevation (m)
RDG11	37.431984	−121.732785	556
RDG12	37.429579	−121.737633	800
RDG13	37.428942	−121.743455	970
RDG14	37.426811	−121.747072	883
RDG21	37.414182	−121.715963	531
RDG22	37.414494	−121.719609	682
RDG23	37.412983	−121.726051	892
RDG24	37.410847	−121.730217	880

because the interstation spacing is small compared to the distances to the sources. For this analysis, the horizontal spectrum is calculated by taking the root mean square (rms) of the two horizontal-component spectra; however, another measure (the HVSR method) is also considered later in the discussion of observational results. The spectral level in a specified frequency band is calculated by taking the geometric average of the individual sampled spectral amplitudes within the frequency limits. Through comparison of spectral amplitudes, we determined that station RDG21 has the lowest amplitude response. This station also occupies the lowest elevation on Poverty Ridge of the eight stations in the array (Fig. 2; Table 1). On this basis, RDG21 is adopted as the reference site for the purpose of calculating relative amplitude ratios. Figure 3 summarizes the horizontal shear-wave spectral ratios in two frequency bands, 0.5–1 Hz and 1–3 Hz. Before the calculation of spectral ratios, all spectra in this study are averaged over a 0.25 Hz bandwidth to smooth the spectra. Each station is given three concentric circles, centered on the station location. The radius of the middle circle is proportional to the geometric mean of the site amplification, averaged over all events recorded at that station and the reference site. The radii of the outer and inner circles are equal to the geometric mean multiplied by and divided by, respectively, the geometric deviation. The length of each spoke is proportional to the amplification for each individual earthquake. The azimuth of the spoke is in the direction of the back azimuth to the source. Three observations are apparent from Figure 3: (1) amplification increases symmetrically with elevation up the ridge, with the largest amplitude at the ridge crest; (2) amplification is greater for sources with back azimuths along the trend of the ridge than for sources lying perpendicular to the ridge axis; and (3) relative amplification at the ridge crest station RDG23 is a factor of 3 and 4 in the two frequency bands 0.5–1 Hz and 1–3 Hz, respectively. Larger amplification moving up the side of the ridge is consistent with the trapping of shear-wave energy in the tapering ridge structure (Geli *et al.*, 1988). The azimuthal dependence of the amplitude has been observed before (Spudich *et al.*, 1996; Panzera *et al.*, 2011) and is due to the favored mode of resonance perpendicular to the trend of the ridge (140°), which is efficiently excited by shear waves from sources along the ridge axis. Using the theoretical

Table 2
Earthquake Sources

Event	yyyy/mm/dd hh:mm	Latitude (°)	Longitude (°)	Magnitude	Depth (km)	Distance (km)	Azimuth
1	2011/06/12 17:07	37.374	−121.731	2.40	7.35	4.34	186.7
2	2011/06/14 11:50	37.375	−121.727	2.98	10.2	4.17	181.7
3	2011/06/21 17:48	37.286	−121.666	2.47	4.95	14.99	159.3
4	2011/08/12 01:46	37.399	−121.764	2.43	3.56	3.72	245.8
5	2011/09/20 16:18	37.464	−121.776	2.41	10.8	7.21	322.1
6	2011/10/10 06:02	37.338	−121.694	2.72	10.1	8.73	161.4
7	2011/10/20 21:40	37.857	−122.252	3.95	8.07	67.7	316.7
8	2011/10/21 03:15	37.861	−122.256	3.84	8.02	68.2	316.8
9	2011/11/02 19:50	37.462	−121.816	2.43	6.92	9.66	304.5
10	2011/11/08 11:56	37.575	−121.973	2.83	9.56	28.30	309.6
11	2011/11/23 16:26	37.384	−121.738	2.72	7.48	3.36	198.7
12	2011/12/03 23:02	37.239	−121.625	2.59	5.33	21.26	155.2
13	2011/12/18 17:46	37.515	−121.846	2.51	7.48	15.55	317.1
14	2011/12/23 05:18	37.873	−122.263	2.75	9.46	69.70	317.2
15	2012/01/01 14:59	37.417	−121.822	2.44	2.77	8.46	273.0
16	2012/01/16 16:41	37.253	−121.637	2.61	5.99	19.34	156.2
17	2012/01/26 02:19	36.935	−121.680	3.39	11.1	53.27	175.6
18	2012/01/26 02:20	36.936	−121.683	3.22	11.0	53.14	175.8
19	2012/02/27 20:04	37.842	−121.910	2.89	10.3	50.36	341.2
20	2012/03/05 13:32	37.926	−122.303	3.44	8.13	76.48	318.3
21	2012/03/05 13:32	37.926	−122.310	3.99	8.12	76.86	318.0
22	2012/03/10 17:22	37.363	−122.157	2.73	7.41	38.47	261.7
23	2012/04/05 08:03	37.258	−121.636	2.65	7.77	18.93	155.3
24	2012/04/05 09:41	37.256	−121.637	2.85	6.26	19.08	155.7
25	2012/04/29 12:52	37.540	−121.922	2.69	9.97	22.34	309.2
26	2012/05/02 02:37	37.084	−122.353	2.90	8.38	66.51	236.6
27	2012/06/03 17:31	37.261	−121.635	3.52	8.46	18.66	154.6

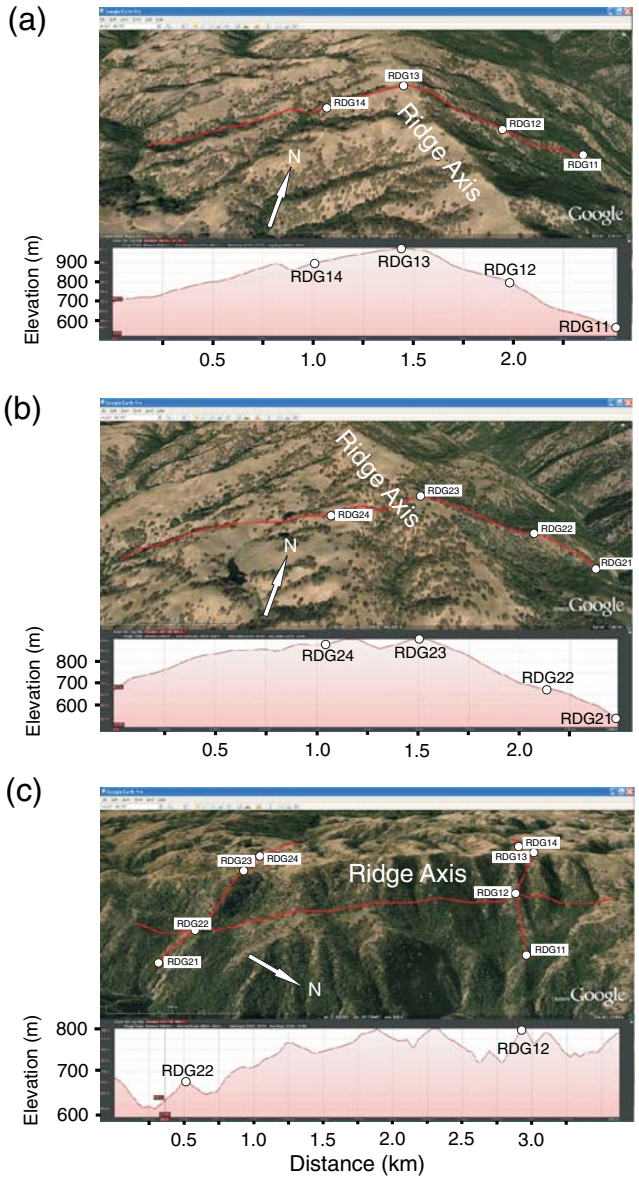

Figure 2. (a) Topographic profile through station line 1, (b) profile through station line 2, and (c) profile at midheight on ridge parallel to main axis of ridge. The color version of this figure is available only in the electronic edition.

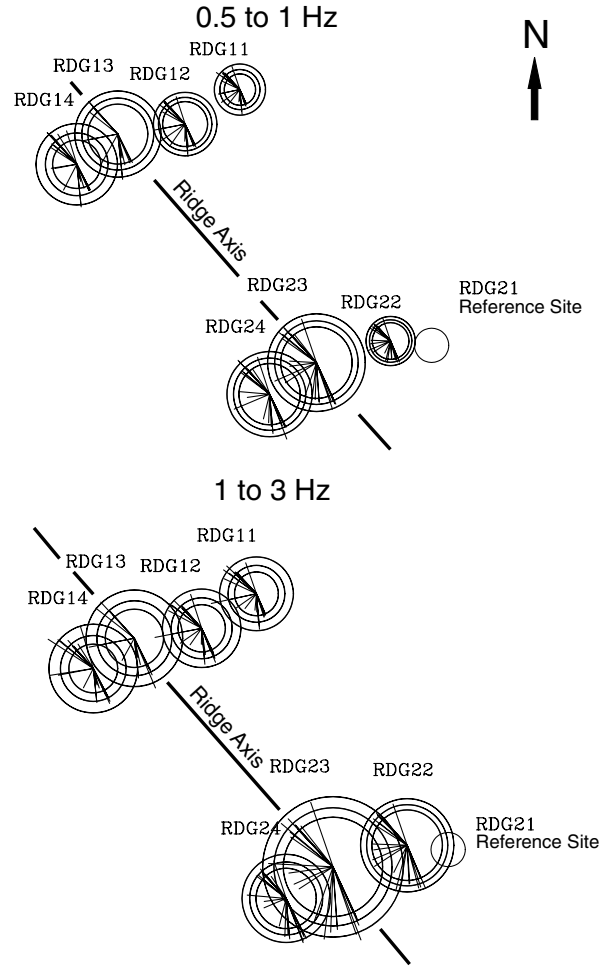

Figure 3. Spectral ratio of the rms of the horizontal components of ground motion at each station relative to the reference site RDG21 at the base of station line 2 for the frequency bands 0.5–1.0 Hz and 1.0–3.0 Hz. The radius of the middle circle in each case is proportional to the geometric mean of the site amplification, averaged over all events recorded at that station and the reference site. The radii of the outer and inner circles are equal to the geometric mean multiplied by and divided by, respectively, the geometric deviation. Spoke length and direction is proportional to the amplification factor and back azimuth for each individual earthquake. The unit amplitude circle given for station RDG21 is for scale.

result that topographic amplification is greatest at the ridge crest for wavelengths equal to the width of the topographic feature (Bouchon, 1973; Geli *et al.*, 1988), we estimate the frequency of maximum amplification to be about $f = V_S/L = 0.625$ Hz, in which $V_S = 1250$ m/s is the velocity of Franciscan rocks at a depth of 150 m (Brocher, 2008) and $L = 2000$ m is the ridge base full width. Given the variability in velocities of Franciscan rocks at shallow depths, this value represents only an estimate; however, the amplification in the 1–3 Hz frequency band does not seem to be associated with the fundamental resonance of the main ridge. Amplification in the 1–3 Hz frequency band is also difficult to associate with shallow deposits, which would require thicknesses of tens of meters. The higher-frequency resonances may be due to higher resonance modes or smaller topographic features.

This same amplification pattern can be seen in the time-domain velocity records in Figure 4. The records are low-pass filtered at 3 Hz. Peak velocity at the ridge crest station (RDG23) is a factor of 2 larger than that for the two symmetrically placed stations part way down on either side of the ridge (RDG22 and RDG24) and a factor of 4 larger than the reference site (RDG21).

Earthquake Ground Motion with the HVSR Method

Arguments have been given that a nonreference site method such as HVSR is better at resolving topographic

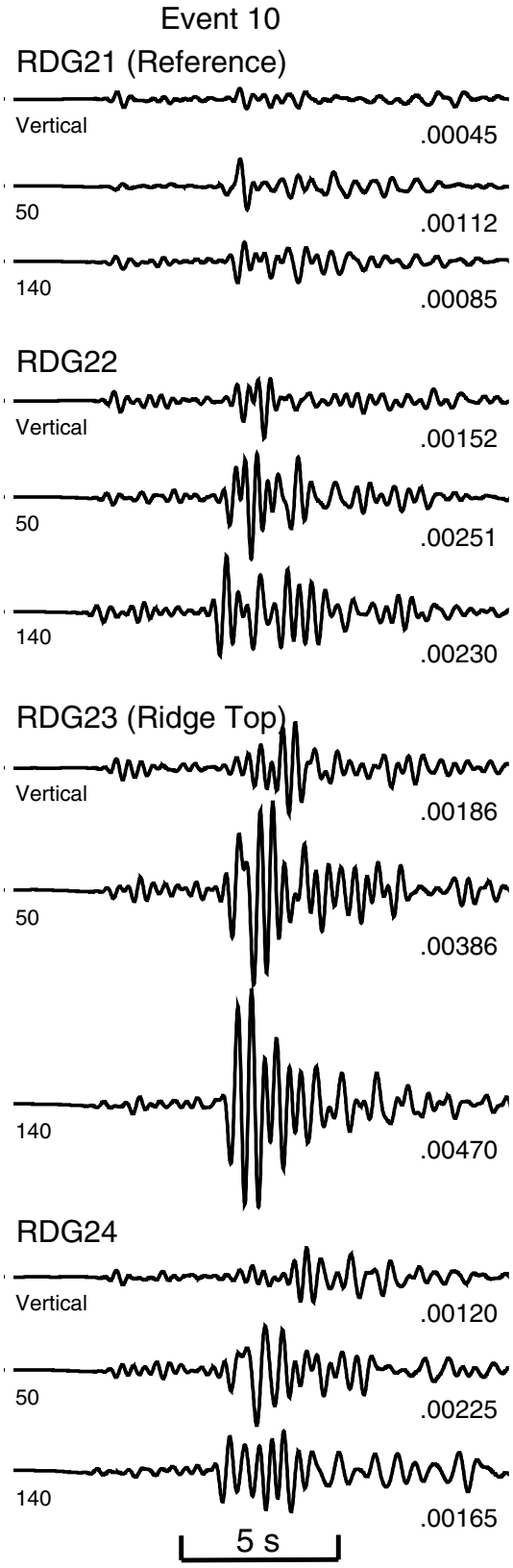

Figure 4. Velocity waveforms for event 10 (Table 2) recorded at station line 2 (Fig. 2b). Horizontal components are rotated to 50° and 140° from north, or approximately perpendicular and parallel with the major trend of Poverty Ridge. Peak amplitudes are given in units of cm/s.

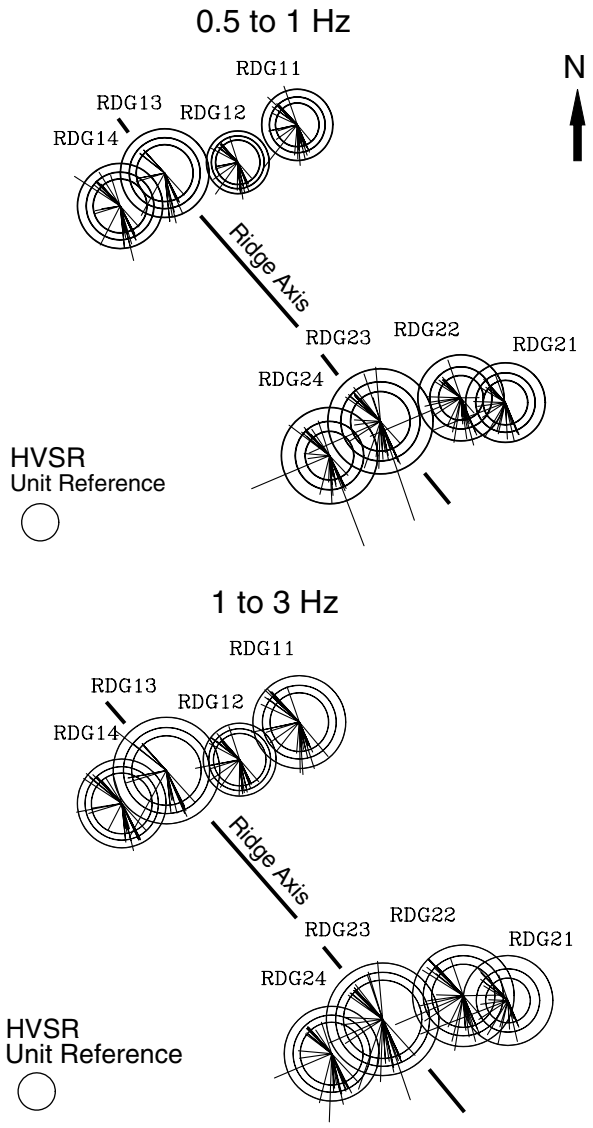

Figure 5. HVSR from earthquake records using the rms of the horizontal components of ground motion for the frequency bands 0.5–1.0 Hz and 1.0–3.0 Hz. Circles show geometric averages over all earthquakes. See the Figure 3 caption for details. Spoke length and direction is proportional to the amplification factor and back azimuth for each individual earthquake. A unit amplitude circle is given for scale.

effects because of the difficulty of obtaining a good reference site near topographic features (Chavez-Garcia *et al.*, 1996, 1997; Panzera *et al.*, 2011). Other studies comparing HVSR with reference site methods have concluded that although HVSR may locate the same fundamental resonance peak, the amplitude is not reliable and other spurious spectral peaks may be introduced (Bonilla *et al.*, 1997; Massa *et al.*, 2010). Figure 5 shows site amplification plotted in the same fashion as Figure 3 using HVSR and the same 43 earthquake records windowed on the shear-wave phase plus coda. The pattern of greater amplification toward the crest of the ridge is much less pronounced. In addition, we do not see as clear of an amplification for sources lying along the trend of the ridge

axis. Therefore, in these two frequency bands HVSR applied to earthquake records did not recover the same spectral characteristics as the reference site method.

The difference between reference site spectral ratios and HVSR is further explored in Figure 6a, in which we compare the spectra for individual events. Figure 6a also shows the result of using an alternative measure for the spectral amplitude of the horizontal motion referred to as maximized spectrum (Shoja-Taheri and Bolt, 1977). This method yields the maximum, as opposed to the rms, amplitude of shaking at a given frequency in the horizontal plane and is formed by treating the two horizontal components of motion (X, Y) as the complex time series, $H(t) = X(t) + iY(t)$ (Lu *et al.*, 1992; Steidl *et al.*, 1996). The amplitude spectrum of the Fourier transform of $H(t)$, normalized by $\sqrt{2}$ for partition of energy between the horizontal components, is used to form the spectral ratio based on the maximized spectrum (Lachet *et al.*, 1996). We conclude from the results in Figure 6a and other event spectra that spectral ratios based on rms and maximum definitions for the horizontal components have similar peaks and troughs but may be different in amplitude. The amplitude differences are not significant to our conclusions, and the same results would be obtained using either spectrum.

Events 10 and 22 (Table 2) were chosen because they lie at azimuths approximately in line with and perpendicular to the major axis of Poverty Ridge, respectively. The reference site ridge-crest-to-base (RDG23/RDG21) ratio for event 10 has the largest amplitudes, consistent with Figure 3 for sources along the trend of the ridge axis. Spectral peaks are seen at approximately 0.9, 2.5, and 5.0 Hz. The HVSR spectrum for event 10 shows the same peaks but generally lower amplitudes and more complicated spectral shapes. The amplitude of the fundamental resonance at 0.9 Hz has the best match in amplitude. For event 22, perpendicular to the ridge axis, the fundamental resonance is poorly developed, with only one prominent peak in our range of interest between 1 and 2 Hz. The amplitude of the crest-to-base spectrum is close to the amplitude of the corresponding HVSR spectrum. These observations are consistent with the efficient trapping of shear-wave energy within the ridge structure by event 10. The fundamental resonance at 0.9 Hz is close to our calculated value for the primary excitation of the ridge at 0.67 Hz, and the higher-frequency spectral peaks are near the expected frequencies for higher modes at multiples of 3 and 5 times the fundament (Williams *et al.*, 2000). The fact that these peaks are not seen or poorly developed at other source azimuths gives further support to the hypothesis that their origin lies in the structure of the ridge. The spectrum for event 22 has a completely different character because these modes are not as effectively excited. Lower amplitude of the HVSR spectra, except for the fundamental resonance, has been observed in other studies (Lermo and Chavez-Garcia, 1993; Lachet *et al.*, 1996; Bonilla *et al.*, 1997). Relative enrichment of the vertical component by scattered waves (Theodulidis *et al.*, 1996) has been offered as an explanation for the generally lower amplitude HVSR spectra, characterized by the omission or randomization of higher-frequency peaks. The spectral peak between 1 and 2 Hz for event 22 may be due to the excitation of another topographic structure of smaller size than the full width of Poverty Ridge. Support for the excitation of smaller structures is given by our analysis of favored directions of ground motion in the Directional Response section.

The azimuthal variability is further delineated in Figure 6b. This figure shows the comparatively smooth variation in the development of the fundamental resonance peak near 1 Hz as a function of azimuth using reference site spectral rations at station RDG23 relative to site RDG21. The 5 frames group spectra within azimuth ranges defined by the availability of sources and progress in a clockwise direction from roughly parallel to the axis of Poverty Ridge (140°), to roughly perpendicular (230°), and back to roughly parallel (320°). As we have noted before, the greater amplitude of the fundamental resonance peak for sources along the strike of the axis of Poverty Ridge is clearly seen.

The robustness of the reference site qualities of station RDG21 is explored in Figure 7. Here, all the rms spectra of the two horizontal components recorded at RDG21 are plotted after normalization at a frequency of 0.5 Hz to adjust for differences in earthquake size and distance. Also plotted as a heavy line is the geometric mean of all the spectra. There is considerable scatter in the individual spectra due to different source characteristics and regional path effects. However, we see no systematic peaks or troughs in the spectra that would be expected from near-surface soils or shallow layering, which should have an effect regardless of the azimuth of the source. Another possible influence on station RDG21 is the effect of adjacent topography. The nearby valley could be the source of deamplification, and multiple adjacent ridges can lead to an increased amplification at the central ridge (Bard, 1982; Geli *et al.*, 1988). These effects are difficult to evaluate given our station configuration but should all be included in our theoretical calculations, which include the topography of the extended region.

Spectra of Ground Motion as a Function of Position

The consistency of the station responses at longer periods (1 s and greater) as a function of height on the ridge can be seen in Figure 8, in which we plot a sampling of well-recorded events. For both station lines 1 and 2 (Fig. 2a,b) the amplitude of the fundamental resonance, which we have identified with the major topographic feature of Poverty Ridge, increases from the lowest station to the crest of the ridge. For most of the events, the amplitudes of the fundamental resonance peak at the lowest stations, RDG11 and RDG21, are near 1 but can be about 2 for some HVSR estimates. Referring to Figure 5, the amplification at the reference site RDG21 averaged over all earthquakes is about a factor of 1.5. The amplitudes at the crest of the ridge, RDG13 and RDG23, are usually between 3 and 4. Above 1 Hz, the spectra become more chaotic. However, events

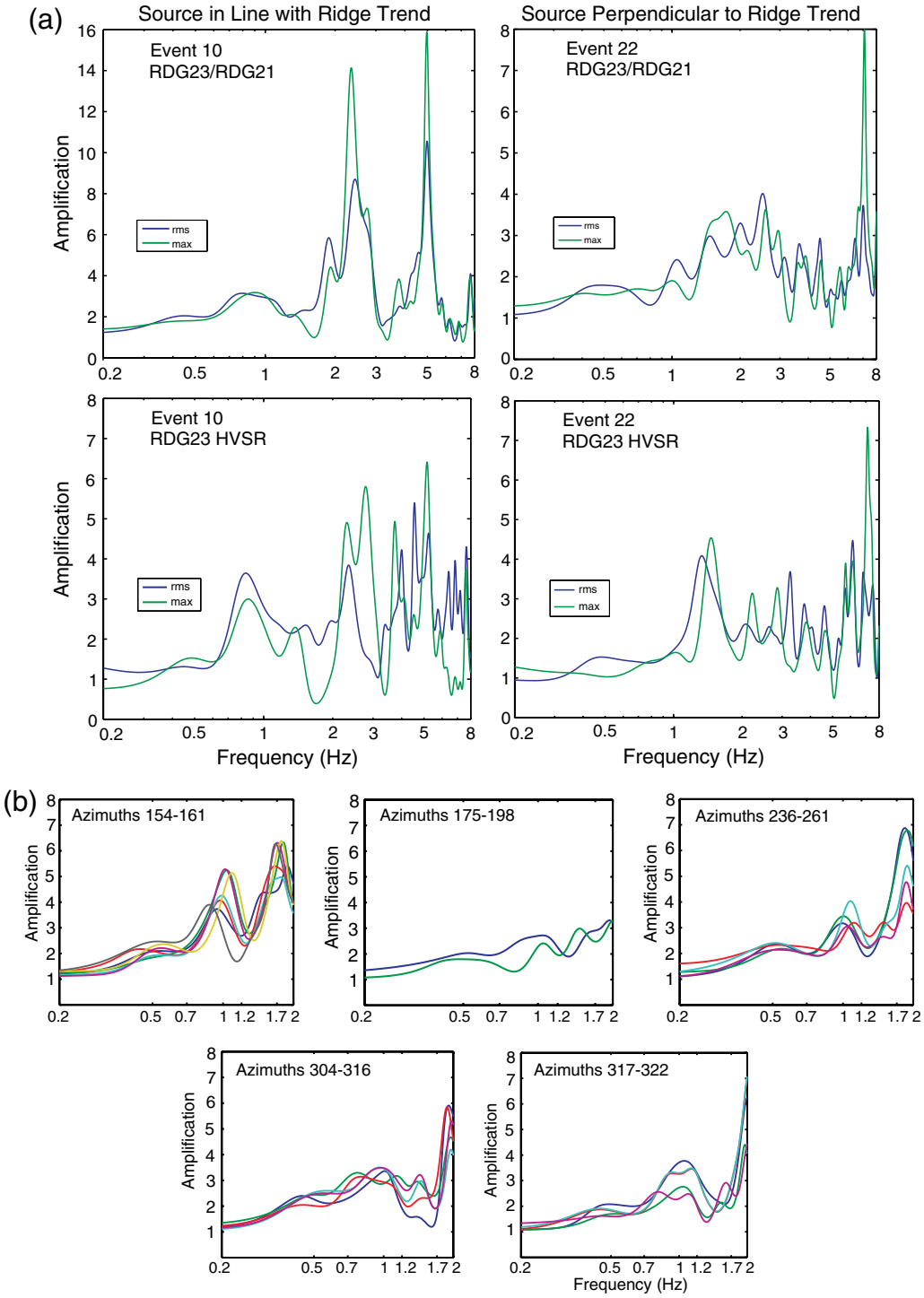

Figure 6. Azimuthal variability of site amplification. (a) Reference site spectral ratios and HVSR using the rms of the horizontal components of ground motion (rms) and the maximum spectrum of the horizontal components (max) (Shoja-Taheri and Bolt, 1977). Event 10 is approximately in line with the major axis of Poverty Ridge, and event 22 is approximately perpendicular. See Figure 1c for the source locations. (b) The fundamental resonance peak near 1 Hz at station RDG23 is relative to reference site RDG21, using the rms of the horizontal components of ground motion. The resonance peak is minimized for sources perpendicular to the major axis of Poverty Ridge (230°). The color version of this figure is available only in the electronic edition.

6, 8, and 10 using the reference site method preserve their relative amplitude ranking observed at lower frequencies up to 3 Hz or more. The HVSR spectra are less orderly above 1 Hz, possibly as a result of the previously mentioned scattered energy on the vertical component. In the Directional Response section, we attempt to explain some of the higher-frequency spectral peaks with directional excitation analysis.

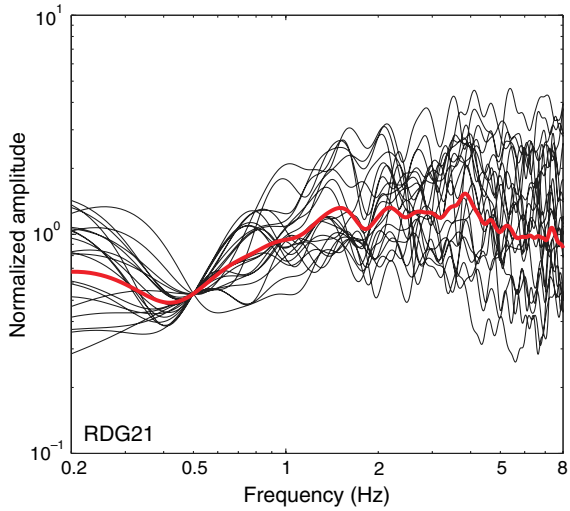

Figure 7. Spectra for the rms of the two horizontal components of earthquake ground motion at the reference site RDG21, normalized to have the same amplitude at a frequency of 0.5 Hz. The heavy curve is the geometric mean of all the individual spectra. The color version of this figure is available only in the electronic edition.

Analysis of Ambient Noise

Ambient noise techniques are well established with wide application to geophysical imaging from continent size crustal velocity models down to local site characterization for site effects (Aki, 1957; Asten and Henstridge, 1984; Louie, 2001; Bensen *et al.*, 2007; Kohler *et al.*, 2007; Moschetti *et al.*, 2007). These techniques rely on the assumption that ambient noise is primarily composed of surface-wave energy, which can be quite different from local earthquake records; however, some investigations have claimed success using HVSR with ambient noise to investigate topographic effects (Lermo and Chavez-Garcia, 1993; Panzera *et al.*, 2011). To further assess the usefulness of ambient noise methods, we perform our own analysis using the continuously recorded channels. We follow the general guidelines of the SESAME Project (SESAME Project, 2004). A stationary record section was selected free of earthquakes, glitches, or other transients. HVSR analysis was performed over 35 continuous 1-minute record segments. The geometric average spectrum is calculated from the 35 samples. Figure 9a,b shows the results for the two lines of stations. Although both lines have the largest amplitudes at the ridge crest stations (RDG13 and RDG23) and the smallest amplitudes at the ridge bottom stations (RDG11 and RDG12), line 2 has responses that are more clearly resolved from one another with an obvious peak near 1 Hz. There is no clear explanation for the difference in behavior between the two lines. The spectral amplitudes based on ambient noise are consistently lower than amplitudes from earthquake records. The general spectral shape for line 2 stations is also a considerably broader feature than seen in most of the earthquake spectra. If the ambient noise in our analysis is dominated by fundamental mode Rayleigh waves, the plots in Figure 9a,b would give the approximate Rayleigh-wave ellipticity. Rayleigh-wave ellipticity has been used to retrieve earth structure (Fah *et al.*, 2001), but its connection to topography is unclear. In addition, because ambient noise typically consists of waves from multiple sources at different azimuths, we do not expect to see the clear spectral peaks observed in the earthquake ground motion.

As another point of comparison, we estimate HVSR from ambient noise using one year of recording. The spectral method is described in detail in McNamara and Buland (2004) and McNamara *et al.* (2014) and is briefly reviewed here. Power spectral density (PSD) is computed from 1 hr time-series segments, overlapping by 50%, from the continuous recording channels. Hourly PSDs are accumulated to form a power density function (PDF). The median of the PDF is taken as the ambient noise level. The HVSR is then calculated using the geometric mean of the medians of the two horizontal components divided by the median of the vertical component PDF. The results are shown in Figure 9c for station line 2. The long-term averages appear to be approximate smoothed versions of the short-term averages shown in Figure 9b.

Figure 9d compares spectra for the ridge crest site RDG23 using the reference site method, HVSR from earthquake data (event 13) and HVSR from ambient noise (1 hr duration). As we noted before, the amplitude of the fundamental resonance is similar for both methods using earthquake ground motion, but the HVSR spectrum has lower amplitude and less coherent peaks at higher frequencies. The ambient noise spectrum appears to be a strongly smoothed version of the other two spectra with only a broad, low-amplitude peak. These observations indicate that although ambient noise may be able to identify the fundamental topographic resonance peak under some circumstances, the amplitude of this peak is unreliable and probably underestimated. The difference between topographic site response estimates from local earthquake records and ambient noise may not be surprising considering that our earthquake records contain a large proportion of body waves and ambient noise is composed of primarily surface waves (Bensen *et al.*, 2007). The angle of incidence of these two wave types is also of importance. As demonstrated by Bard (1982), the topographic effect decreases as the angle of incidence increases. Surface propagating waves are not expected to have the same interaction with a topographic feature as near vertically incident body waves.

Directional Response

There is considerable observational and theoretical evidence that the primary oscillatory mode for topography is transverse to the main axis of a ridge (Bouchon and Barker, 1996; Spudich *et al.*, 1996; Panzera *et al.*, 2011). In addition, resonances from shallow structures in the absence of topography have also been shown to display favored directions of excitation (Hartzell *et al.*, 1997, 2000). To investigate the directional response at Poverty Ridge we calculate the relative

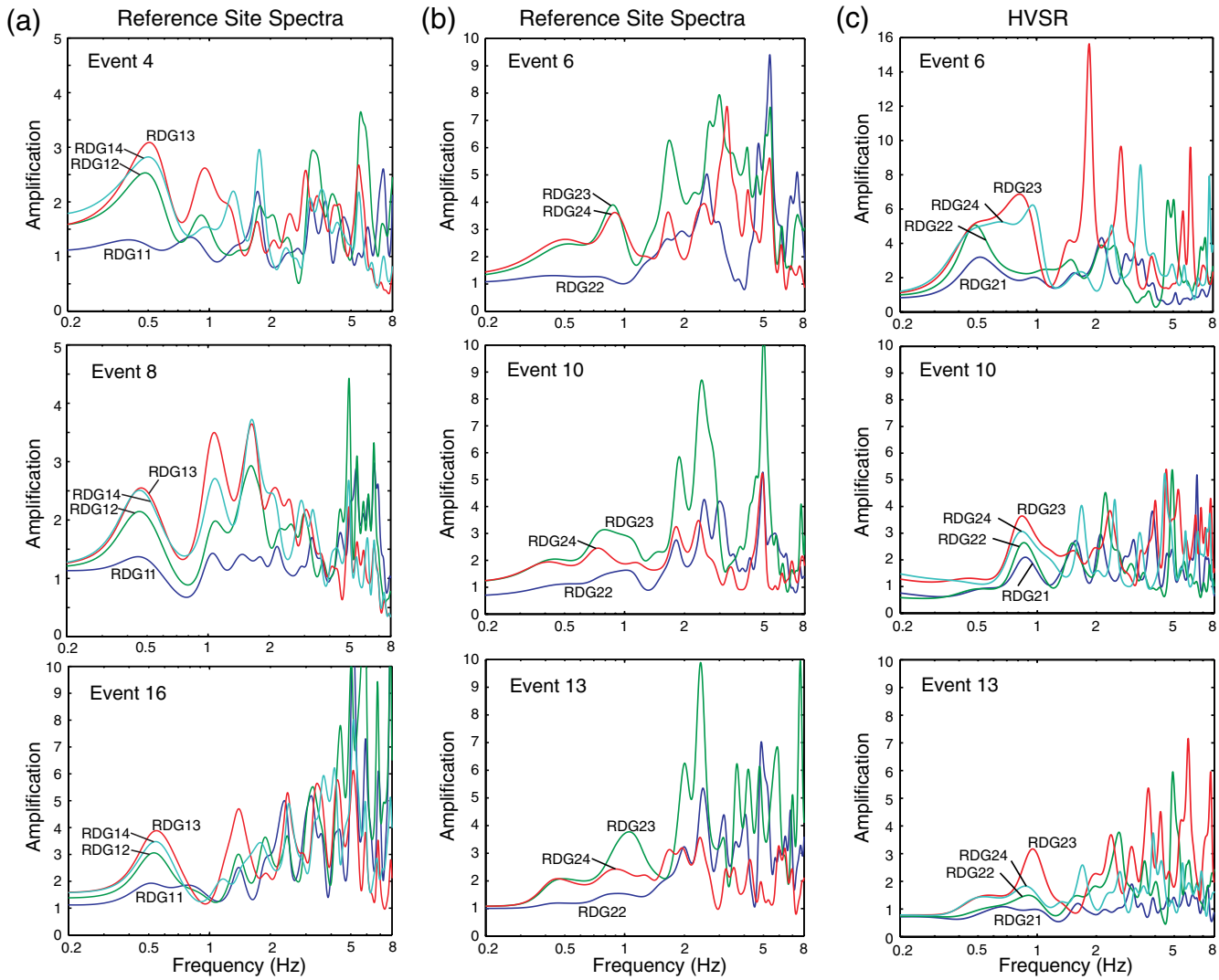

Figure 8. Earthquake-based amplification spectra as a function of position on Poverty Ridge using (a) rms of horizontal components relative to the reference site RDG21 for station line 1, (b) rms of horizontal components relative to the reference site RDG21 for station line 2, and (c) HVSR for station line 2. See Table 2 and Figure 1c for information on earthquake locations. The color version of this figure is available only in the electronic edition.

site response as a function of azimuth by successively rotating the horizontal components into different compass directions at 5° increments. As before, the reference site is RDG21, the lowest station on the ridge. Spectra are calculated for the shear wave plus coda segment from each earthquake in our data set recorded at a particular site. The geometric mean of the individual spectra is then calculated for each azimuth. The directional site response plots are shown in Figure 10 for the stations in line 1. There is a first order difference between the stations on the flanks of Poverty Ridge (RDG11, RDG12, and RDG14) and the station at the ridge crest (RDG13). The primary mode of excitation of the ridge-flanking stations is at an azimuth around 120° and at higher frequencies between 3 and 6 Hz. Referring to Figure 2c, we see that Poverty Ridge is characterized by deeply cut canyons that are separated by prominent ribs running the full height of the main ridge. Our stations are located on these ribs. The base width of the rib used for station line 1 can be interpreted as between 200 and 500 m, depending on the breadth of the rib structure. For V_S of 1250 m/s, these values yield a range in frequencies for the fundamental resonance from 2.5 to 6.25 Hz. This estimated range may explain the vertical elongation over a range in frequencies of the maximum amplitudes seen for sites RDG11, RDG12, and RDG13 in Figure 10. In addition, the direction of this excitation is approximately perpendicular to the trend of the ribs, as is expected. The maximum amplification for station RDG13 at the ridge crest occurs at lower frequencies between 1 and 3 Hz and at lower azimuthal angles more consistent with excitation of the primary axis of Poverty Ridge. However, this site also shows some energy in the frequency and azimuth range of the rib structures, indicating a complex interaction between these different topographic features. Some of the complexity we have seen in the individual

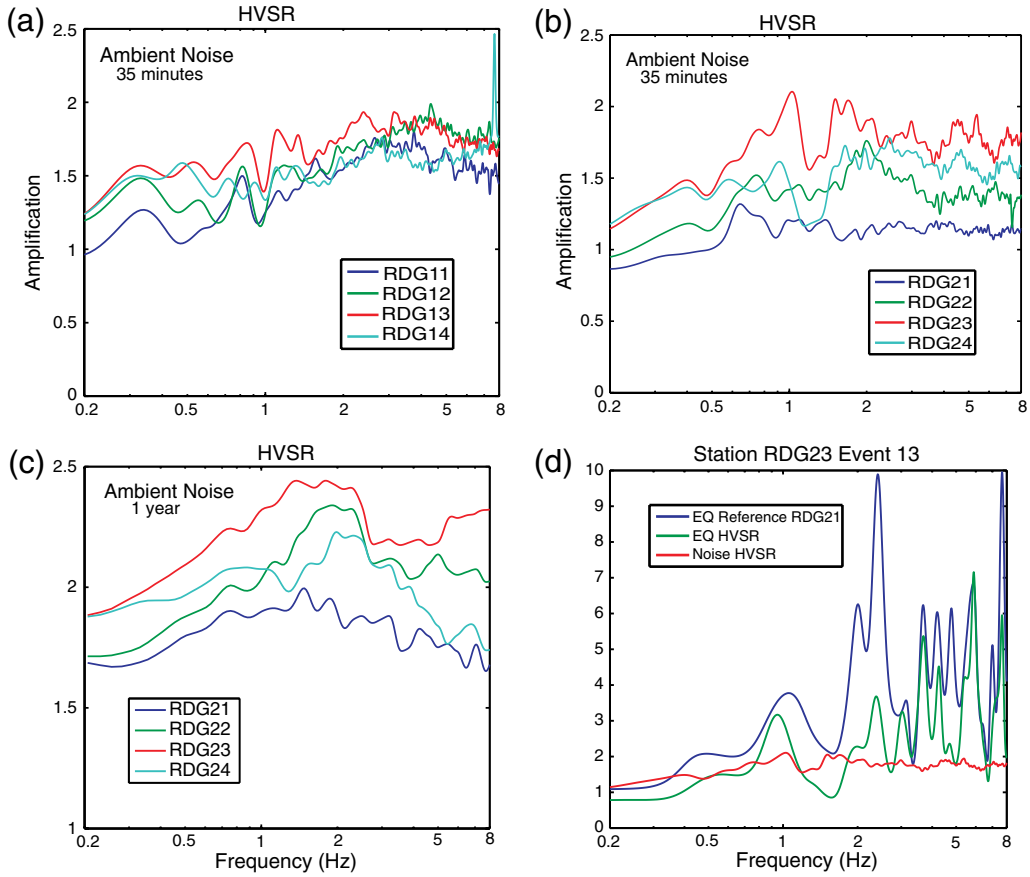

Figure 9. (a, b) HVSR as a function of position on Poverty Ridge, using 35 min of ambient noise for station lines 1 and 2, (c) HVSR as a function of position on Poverty Ridge, using 1 yr of ambient noise for station line 2, (d) comparison between earthquake based amplification spectra at the ridge crest station RDG23, using the reference site method, earthquake-based spectra using the HVSR method, and the HVSR method using ambient noise. The color version of this figure is available only in the electronic edition.

spectra at frequencies above the fundamental resonance of Poverty Ridge may be due to other topographic effects from substructures composing the main ridge.

Theoretical Calculations

The topographic effects of Poverty Ridge are modeled using a previously verified 3D octree-based finite-element solver (Tu *et al.*, 2006; Bielak *et al.*, 2010) capable of modeling topography. We use the U.S. Geological Survey (USGS) Bay Area Velocity Model 08.3.0 (see Data and Resources) with the Q_s attenuation model from Hartzell *et al.* (2006). The velocity model is augmented using topography from the 1/3 arc second USGS DEM of the region (see Data and Resources). Topography is approximated in the finite-element grid with a staircase free surface (Pitarka and Irikura, 1996; Koketsu *et al.*, 2004) and cubic elements with 12 points per wavelength and an element size of 12.2 m to avoid inaccuracies in the linear elements employed in the simulations. A regional view of the model's near-surface shear-wave velocities can be seen in Hartzell *et al.* (2010). The 1D velocity profile down through Poverty Ridge taken from this 3D model is shown in Figure 11. This profile is the same for the entirety of Poverty Ridge. The velocity model contains no near-surface soil layer or shallow velocity interfaces that would lead to resonances. Therefore, theoretical differences in site response obtained from this model must be primarily attributed to the configuration of the ridge. We model two point sources, one approximately in line with the major axis of Poverty Ridge (S1: 37.4642, −121.7762) and another at an angle of 50° to the trend of the ridge (S2: 37.4170, −121.8218). See Figure 1a for the source locations. Each source is at a depth of 7 km and distance of about 8 km from Poverty Ridge. Although we are not attempting to model specific earthquakes, we use a mechanism for both sources consistent with earthquakes on the Calaveras fault with strike = 323°, dip = 87°, and rake = 180°. The slip-rate function for both sources is a 0.1 s duration isosceles triangle. Both simulations are done to an upper frequency limit of 3 Hz.

The maximum of the vector sum of the two horizontal components of ground velocity is plotted in Figure 12 over the topography for the two sources, S1 and S2. Greater excitation is clearly seen along the major ridge crest as well as the lateral ribs. The amplification in these areas is between a factor of 3 and 4 relative to the base of the ridge. These

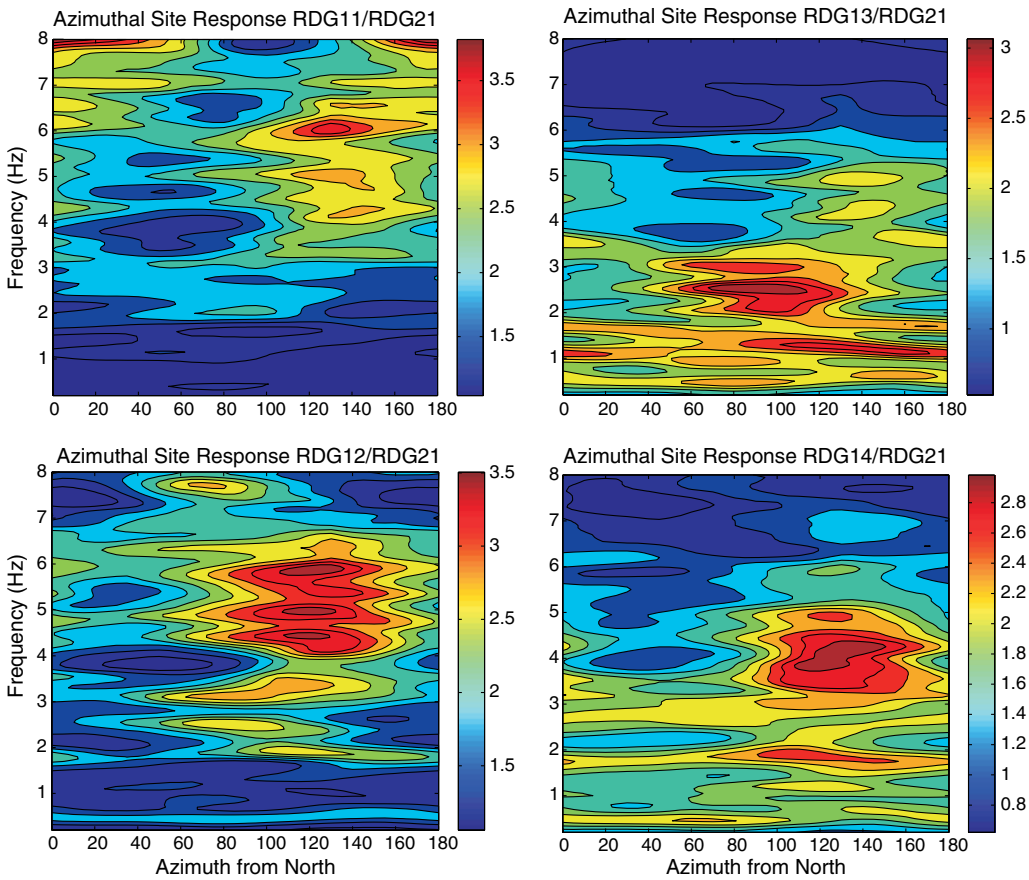

Figure 10. Earthquake ground-motion directional response as a function of position on Poverty Ridge for station line 1. Spectra are calculated using the rms of the two horizontal components of ground motion and the reference site method relative to station RDG21. The amplification factor is given by the graded scale to the right of each frame. The color version of this figure is available only in the electronic edition.

values are in good agreement with the amplification seen in the data records in Figures 3 and 8. These two simulations demonstrate some of the wide-ranging variability in ground motion that results for different source locations. Source S1 along the major axis of the ridge causes significant amplification of ground motion down the full length of the ridge due to the efficient trapping of waves within the ridge structure. In contrast, source S2 at a 50° angle to the axis of the ridge amplifies ground motion significantly more for station line 1 than line 2. Also apparent from Figure 12 is the rapid spatial variation in ground motion. Peak velocity can change by a factor of 2 over a distance as short as 100 m.

We examine the relative amplification spectra of the synthetic ground motion in Figure 13. As with the earthquake records, the reference site is RDG21, the lowest station in the array. First, the fundamental resonance peak is clearly observed at a frequency of 0.5–0.65 Hz. This frequency range compares very well with the frequency of the fundamental resonance seen in Figure 8a for station line 1. For station line 2, the fundamental resonance peak of the data

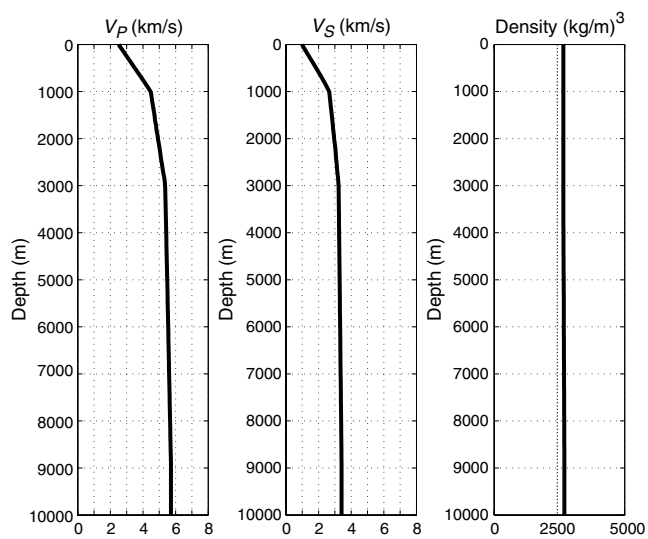

Figure 11. Model parameters for a 1D profile through the crest of Poverty Ridge, taken from the 3D velocity model used in the finite-element simulation of ground motion.

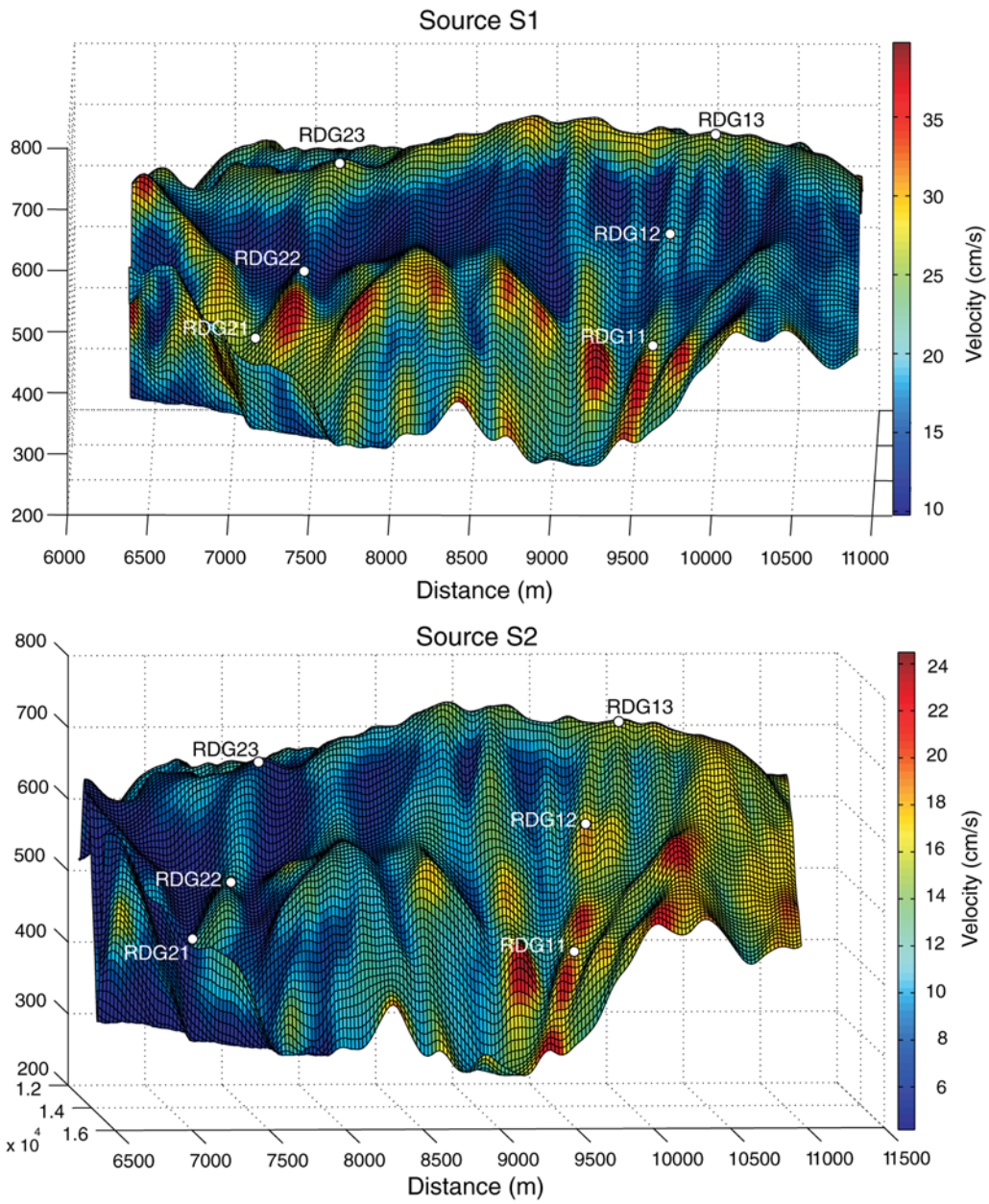

Figure 12. A finite-element calculation of the maximum value of the vector sum of the two horizontal components of ground velocity plotted over the topography of Poverty Ridge for sources S1 and S2. See Figure 1a for the source locations. The view is from the northeast. Station locations are indicated by dots. All distance scales are in meters. The color version of this figure is available only in the electronic edition.

also occurs at 0.5 Hz but is more subtle, with a more prominent spectral peak near 1 Hz (Fig. 8b). This 1 Hz peak can also be seen in the spectra of the synthetic records for source S2. The relative amplitudes of the stations progressing up the slope of the ridge are the same in the data and the synthetics. Both the data and the synthetic spectra also show fairly consistent peak amplitudes at the ridge crest of 2.5–3.5 times the base amplitude. The greatest difference between the observed and synthetic spectra lies in the amplitude of resonance peaks above 1 Hz. As we noted earlier, large amplitude, higher-frequency spectral peaks are observed in the data, primarily for sources in line with the major axis of the ridge, such as for event 10 in Figure 8b. We also see an indication of these higher frequency peaks in the synthetic spectra in Figure 13 for source S1 in line with the ridge axis. Although of lower amplitude, peaks are seen at frequencies of 2 and 3 Hz for source S1, but not for the off-axis source S2. Modeling the amplitude of the higher-frequency spectral peaks correctly places a greater demand on the accuracy of the 3D velocity and topography model that may not be attained. Also, we know that considerable variability in ground motion exists with changing source location and depth. Our

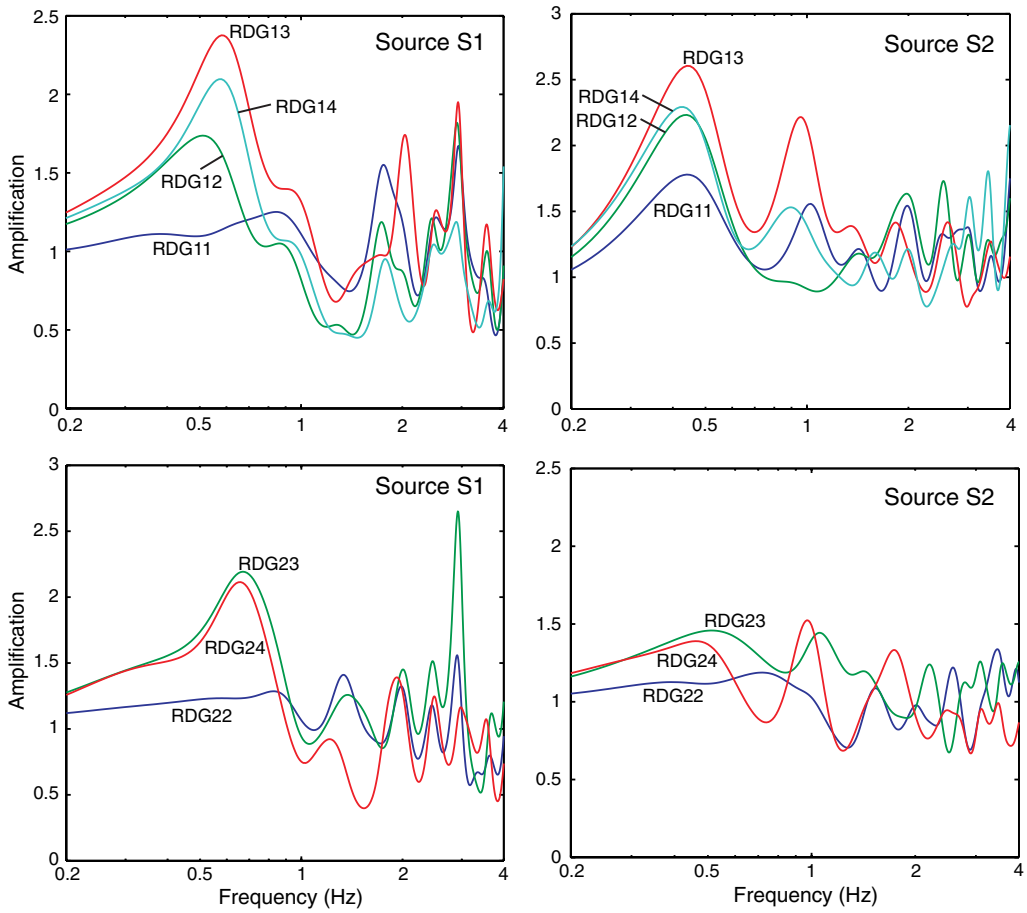

Figure 13. Horizontal spectral ratios based on the rms of the two horizontal components of ground motion and the reference site RDG21 from finite-element simulations of sources S1 and S2. See Figure 1a for the source locations. The color version of this figure is available only in the electronic edition.

two simulated sources do not capture the full range in possible ground motions. Other authors have pointed out the complexities that can be a part of site response caused by 3D stratigraphic irregularities (Paolucci *et al.*, 1999; Assimaki *et al.*, 2005; and Graizer, 2009). We have argued that such irregularities are minimal in the structure of Poverty Ridge, but they could still have an effect on higher frequencies above the fundamental resonance.

Conclusions

Previous studies of topographic effects have shown a general pattern of underprediction of amplification factors from theoretical calculations compared with the amplification seen in data records. Our results show that the amplitude of the fundamental resonance peak can be well predicted using an accurate 3D digital elevation model and velocity model. However, this conclusion needs to be tempered with the fact that ground motion on topography is sensitive to the direction of approach and polarization of the incoming waves, particularly at frequencies above the fundamental resonance. Although there is an indication of the same spectral peaks above the fundamental resonance in the theoretical spectra as in the observed spectra for sources approximately in line with the major axis of the ridge, the amplitude of these peaks were underpredicted. The ground motion from our two simulations does not encompass all source distances and azimuths, and different results are likely from the study of other source locations. However, our results support the use of topography in ground-motion simulations to obtain more accurate predictions of earthquake ground motions up through the fundamental resonance frequency of the topographic feature.

Poverty Ridge shows a ridge-crest amplification of a factor of 3–4 at the fundamental resonance of approximately 0.5–1.0 Hz relative to a ridge-base site. The frequency of the fundamental resonance can shift with the azimuth and angle of incidence of the incoming waves, probably as a result of a more favorable resonance over a different ridge dimension. Reference site spectral ratios are found to be the most robust at defining the amplitude of the fundamental resonance, as well as the frequency and amplitude of higher-frequency resonances. HVSR analysis of earthquake records usually recovers the frequency and amplitude of the fundamental resonance but does not show higher-frequency peaks, possibly

due to increased scattered wave energy on the vertical component. Ambient noise is found to be a poor source for the study of topographic effects. Spectral ratios over topography from ambient noise are broad functions of frequency with lower amplitude than spectra from earthquakes. These observations are probably due to the dominance of surface waves in ambient noise, as contrasted with body waves in local earthquake records and the averaging over azimuth of ambient noise sources. Strong directionality is seen in the topographic resonance frequencies that are transverse to the major axes of the topographic features.

Data and Resources

The elevation data are derived using the 1/3 arc second USGS digital elevation model of the region, available at http://nationalmap.gov/viewer.html (last accessed December 2012). The 3D velocity model is available from the USGS website http://earthquake.usgs.gov/research/structure/3dgeologic (last accessed December 2012). These databases have been approved for release and publication by the USGS. Although these databases have been subjected to rigorous review and are substantially complete, the USGS reserves the right to revise the data pursuant to further analysis and review. Furthermore, they are released on condition that neither the USGS nor the U.S. Government may be held liable for any damages resulting from its authorized or unauthorized use. The ground-motion data are available from the Incorporated Research Institute for Seismology (IRIS), http://www.iris.edu (last accessed December 2012). Images of the study area are from 2013 Google Earth.

Acknowledgments

This study would not have been possible without the generous cooperation of the property owners: The San Francisco Public Utilities Commission, The Nature Conservancy, and Bill Nelson. The often strenuous field work was performed by personnel from the USGS in Golden, Colorado (Mark Meremonte, Alena Leeds, Daniel Bowden, Erin Beck), in Menlo Park, California (Max Gardner, Alex Ferguson, Neil Fenning, Katharine Turkle, Josh Quisenberry, John Brockman), and in Albuquerque, New Mexico (Steve Ploetz). Any use of trade, firm, or product names is for descriptive purposes only and does not imply endorsement by the U.S. Government.

References

Aki, K. (1957). Space and time spectra of stationary stochastic waves, with special reference to microtremors, *Bull. Earthq. Res. Inst. Tokyo Univ.* **35,** 415–457.

Aki, K., and K. L. Larner (1970). Surface motion of a layered medium having an irregular interface due to incident plane *SH* waves, *J. Geophys. Res.* **75,** 933–954.

Assimaki, D., G. Gazetas, and E. Kausel (2005). Effects of local soil conditions on the topographic aggravation of seismic motion: Parametric investigation and recorded field evidence from the 1999 Athens earthquake, *Bull. Seismol. Soc. Am.* **95,** 1059–1089.

Asten, M. W., and J. D. Henstridge (1984). Array estimators and the use of microseisms for reconnaissance of sedimentary basins, *Geophysics* **49,** 1828–1837.

Bard, P.-Y. (1982). Diffracted waves and displacement field over two-dimensional elevated topographies, *Geophys. J. Roy. Astron. Soc.* **71,** 731–760.

Bensen, G. D., M. H. Ritzwoller, M. P. Barmin, A. L. Levshin, F. Lin, M. P. Moschetti, N. M. Shapiro, and Y. Yang (2007). Processing seismic ambient noise data to obtain reliable broad-band surface wave dispersion measurements, *Geophys. J. Int.* **169,** 1239–1260.

Bielak, J., R. W. Graves, K. B. Olsen, R. Taborda, L. Ramirez-Guzman, S. M. Day, G. P. Ely, D. Roten, T. H. Jordan, P. J. Maechling, J. Urbanic, and G. Juve (2010). The ShakeOut earthquake scenario: Verification of three simulation sets, *Geophys. J. Int.* **180,** 375–404.

Bonilla, L. F., J. H. Steidl, G. T. Lindley, A. G. Tumarkin, and R. J. Archuleta (1997). Site amplification in the San Fernando Valley, California: Variability of site-effect estimation using the *S*-wave, coda, and H/V methods, *Bull. Seismol. Soc. Am.* **87,** 710–730.

Boore, D. M. (1972). A note on the effect of simple topography on seismic *SH* waves, *Bull. Seismol. Soc. Am.* **62,** 275–284.

Bouchon, M. (1973). Effect of topography on surface motion, *Bull. Seismol. Soc. Am.* **63,** 615–632.

Bouchon, M., and J. S. Barker (1996). Seismic response of a hill: The example of Tarzana, California, *Bull. Seismol. Soc. Am.* **86,** 66–72.

Bouchon, M., C. A. Schultz, and M. N. Toksoz (1996). Effect of three-dimensional topography on seismic motion, *J. Geophys. Res.* **101,** 5835–5846.

Brocher, T. M. (2008). Compressional and shear-wave velocity versus depth relations for common rock types in northern California, *Bull. Seismol. Soc. Am.* **98,** 950–968.

Chavez-Garcia, F. J., M. Rodriguez, E. H. Field, and D. Hatzfeld (1997). Topographic site effects. A comparison of two nonreference methods, *Bull. Seismol. Soc. Am.* **87,** 1667–1673.

Chavez-Garcia, F. J., L. R. Sanchez, and D. Hatzfeld (1996). Topographic site effects and HVSR. A comparison between observations and theory, *Bull. Seismol. Soc. Am.* **86,** 1559–1573.

Davis, L. L., and L. R. West (1973). Observed effects of topography on ground motion, *Bull. Seismol. Soc. Am.* **63,** 283–298.

Fah, D., F. Kind, and D. Giardini (2001). A theoretical investigation of average H/V ratios, *Geophys. J. Int.* **145,** 535–549.

Geli, L., P.-Y. Bard, and B. Jullien (1988). The effect of topography on earthquake ground motion: A review and new results, *Bull. Seismol. Soc. Am.* **78,** 42–63.

Graizer, V. (2009). Low-velocity zone and topography as a source of site amplification effect on Tarzana hill, California, *Soil Dynam. Earthq. Eng.* **29,** 324–332.

Griffiths, D. W., and G. A. Bollinger (1979). The effect of Appalachian Mountain topography on seismic waves, *Bull. Seismol. Soc. Am.* **69,** 1081–1105.

Hartzell, S., D. Carver, E. Cranswick, and A. Frankel (2000). Variability of site response in Seattle, Washington, *Bull. Seismol. Soc. Am.* **90,** 1237–1250.

Hartzell, S., E. Cranswick, A. Frankel, D. Carver, and M. Meremonte (1997). Variability of site response in the Los Angeles urban area, *Bull. Seismol. Soc. Am.* **87,** 1377–1400.

Hartzell, S., S. Harmsen, R. A. Williams, D. Carver, A. Frankel, G. Choy, P.-C. Liu, R. C. Jachens, T. M. Brocher, and C. M. Wentworth (2006). Modeling and validation of a 3D velocity structure for the Santa Clara Valley, California, for seismic-wave simulations, *Bull. Seismol. Soc. Am.* **96,** 1851–1881.

Hartzell, S., L. Ramirez-Guzman, D. Carver, and P.-C. Liu (2010). Short baseline variations in site response and wave-propagation effects and their structural causes: Four examples in and around the Santa Clara Valley, California, *Bull. Seismol. Soc. Am.* **100,** 2264–2286.

Kohler, A., M. Ohrnberger, F. Scherbaum, M. Wathelet, and C. Cornou (2007). Assessing the reliability of the modified three-component spatial autocorrelation technique, *Geophys. J. Int.* **168,** 779–796.

Koketsu, K., H. Fujiwara, and Y. Ikegami (2004). Finite-element simulation of seismic ground motion with a voxel mesh, *Pure Appl. Geophys.* **161,** 2183–2198.

Lachet, C., D. Hatzfeld, P.-Y. Bard, N. Theodulidis, C. Papaioannou, and A. Savvaidis (1996). Site effects and microzonation in the city of Thessaloniki (Greece) comparison of different approaches, *Bull. Seismol. Soc. Am.* **86,** 1692–1703.

Lee, S.-J., Y.-C. Chan, D. Komatitsch, B.-S. Huang, and J. Tromp (2009). Effects of realistic surface topography on seismic ground motion in the Yangminshan region of Taiwan based upon the spectral-element method and LiDAR DTM, *Bull. Seismol. Soc. Am.* **99,** 681–693.

Lee, S.-J., D. Komatitsch, B.-S. Huang, and J. Tromp (2009). Effects of topography on seismic-wave propagation: An example from northern Taiwan, *Bull. Seismol. Soc. Am.* **99,** 314–325.

Lermo, J., and F. J. Chavez-Garcia (1993). Site effect evaluation using spectral ratios with only one station, *Bull. Seismol. Soc. Am.* **83,** 1574–1594.

Louie, J. N. (2001). Faster, better: Shear-wave velocity to 100 meters depth from refraction microtremor arrays, *Bull. Seismol. Soc. Am.* **91,** 347–364.

Lu, L., F. Yamazaki, and T. Katayama (1992). Soil amplification based on seismometer array and microtremor observations in Chiba, Japan, *Earthq. Eng. Struct. Dynam.* **21,** 95–108.

Ma, S., R. J. Archuleta, and M. T. Page (2007). Effects of large-scale surface topography on ground motions, as demonstrated by a study of the San Gabriel Mountains, Los Angeles, California, *Bull. Seismol. Soc. Am.* **97,** 2066–2079.

Massa, M., S. Lovati, E. D'Alema, G. Ferretti, and M. Bakavoli (2010). An experimental approach for estimating seismic amplification effects at the top of a ridge, and the implication for ground-motion predictions: The case of Narni, Central Italy, *Bull. Seismol. Soc. Am.* **100,** 3020–3034.

McNamara, D., and R. Buland (2004). Ambient noise levels in the continental United States, *Bull. Seismol. Soc. Am.* **94,** 1517–1527.

McNamara, D., L. Gee, H. Benz, and M. Chapman (2014). Frequency dependent seismic attenuation in the eastern US as observed from the 2011 central Virginia earthquake and aftershock sequence, *Bull. Seismol. Soc. Am.* **104,** doi: 10.1785/0120130045.

Moschetti, M. P., M. H. Ritzwoller, and N. M. Shapiro (2007). Surface wave tomography of the western United States from ambient seismic noise: Rayleigh wave group velocity maps, *Geochem. Geophys. Geosys.* **8,** Q08010, doi: 10.1029/2007GC001655.

Panzera, F., G. Lombardo, and R. Rigano (2011). Evidence of topographic effects through the analysis of ambient noise measurements, *Seismol. Res. Lett.* **82,** 413–419.

Paolucci, R., E. Faccioli, and F. Maggio (1999). 3D response analysis of an instrumented hill at Matsuzaki, Japan, by a spectral method, *J. Seismol.* **3,** 191–209.

Pedersen, H., B. Le Brun, D. Hatzfeld, M. Campillo, and P.-Y. Bard (1994). Ground-motion amplitude across ridges, *Bull. Seismol. Soc. Am.* **84,** 1786–1800.

Pitarka, A., and K. Irikura (1996). Modeling 3D surface topography by finite-difference method: Kobe-JMA station site, Japan, case study, *Geophys. Res. Lett.* **23,** 2729–2732.

Rogers, A. M., L. J. Katz, and T. J. Bennett (1974). Topographic effects on ground motion for incident *P* waves: A model study, *Bull. Seismol. Soc. Am.* **64,** 437–456.

Sánchez-Sesma, F. J., and M. Campillo (1991). Diffraction of *P*, *SV*, and Rayleigh waves by topographic features: A boundary integral formulation, *Bull. Seismol. Soc. Am.* **81,** 2234–2253.

Sato, R. (1955). Reflection of elastic waves at a corrugated free surface (in Japanese), *J. Seismol. Soc. Japan* **8,** 121.

SESAME Project (2004). Guidelines for the implementation of the H/V spectral ratio technique on ambient vibrations: Measurements, processing and interpretation, SESAME European Reseach Project WP12; deliverable no. D23.12; http://www.geopsy.org (last accessed October 2013).

Shoja-Taheri, J., and B. A. Bolt (1977). A generalized strong-motion accelerogram based on spectral maximization from two horizontal components, *Bull. Seismol. Soc. Am.* **67,** 863–876.

Spudich, P., M. Hellweg, and W. H. K. Lee (1996). Directional topographic site response at Tarzana observed in aftershock of the 1994 Northridge, California, earthquake: Implications for mainshock motions, *Bull. Seismol. Soc. Am.* **86,** S193–S208.

Steidl, J. H., A. G. Tumarkin, and R. J. Archuleta (1996). What is a reference site? *Bull. Seismol. Soc. Am.* **86,** 1733–1748.

Theodulidis, N., P.-Y. Bard, R. Archuleta, and M. Bouchon (1996). Horizontal-to-vertical spectral ratio and geological conditions: The case of Garner Valley downhole array in southern California, *Bull. Seismol. Soc. Am.* **86,** 306–319.

Tu, T., H. Yu, L. Ramirez-Guzman, J. Bielak, O. Ghattas, K. L. Ma, and D. O'Hallaron (2006). From mesh generation to scientific visualization: An end-to-end approach to parallel supercomputing, *Proc. of the 2006 ACM/IEEE Conference on Supercomputing*, Tampa, Florida, 11–17 November 2006, 12 pp.

Williams, R. A., W. J. Stephenson, A. D. Frankel, E. Cranswick, M. E. Meremonte, and J. K. Odum (2000). Correlation of 1- to 10-Hz earthquake resonances with surface measurements of *P*- and *S*-wave reflections and refractions in the upper 50 m, *Bull. Seismol. Soc. Am.* **90,** 1323–1331.

US Geological Survey
Denver Federal Center
Box 25046, MS 966
Denver, Colorado 80225
(S.H., M.M., D.M.)

Instituto de Ingeniería (UNAM)
Edificio 1 Cubiculo 108
Ciudad Universitaria, Coyoacán
Mexico D.F., C.P. 04510
(L.R.-G.)

Manuscript received 17 April 2013;
Published Online 19 November 2013